A New Model for Void Coalescence by Internal Necking

F. Scheyvaerts and T. Pardoen*
Institute of Mechanics, Materials and Civil Engineering, Université catholique de Louvain, Place Sainte Barbe 2, B-1348 Louvain-la-Neuve, Belgium

P. R. Onck
Micromechanics of Materials, Zernike Institute for Advanced Materials, University of Groningen, Nijenborgh 4, 9747 AG Groningen, The Netherlands

ABSTRACT: A micromechanical model for predicting the strain increment required to bring a damaged material element from the onset of void coalescence up to final fracture is developed based on simple kinematics arguments. This strain increment controls the unloading slope and the energy dissipated during the final step of material failure. Proper prediction of the final drop of the load carrying capacity is an important ingredient of any ductile fracture model, especially at high stress triaxiality. The model has been motivated and verified by comparison to a large set of finite element void cell calculations.

KEY WORDS: metals, micromechanics, ductile fracture, void coalescence.

INTRODUCTION

Void coalescence is the most common fracture initiation mechanism in ductile metals. It consists of a transition from a phase of diffuse plastic deformation driving the stable growth of small internal voids to a localized mode of plastic deformation within the ligament separating two voids or a row of voids, with material off the localization plane usually undergoing elastic unloading. Although predicting when this final step in the damage process starts and how fast it develops is crucial, most of the efforts carried on by the fracture community in this field during the 80' and 90's has

*Author to whom correspondence should be addressed. E-mail: thomas.pardoen@uclouvain.be
Figure 4 appears in color online: http://ijd.sagepub.com

1056-7895/10/01 0095–32 $10.00/0 DOI: 10.1177/1056789508101918

focused on improving and extending void growth models and associated computational schemes (e.g., Gurson, 1977; Tvergaard, 1981, 1990; Needleman and Tvergaard, 1984; Tvergaard and Needleman, 1984; Mear and Hutchinson, 1985; Marini et al., 1985; Becker et al., 1988, 1989; Koplik and Needleman, 1988; Hom and McMeeking, 1989; Gologanu et al., 1993, 1994, 1997; Leblond et al., 1994, 1995; Xia and Shih, 1995a,b; Xia et al., 1995; Ruggieri et al., 1996; Steglich and Brocks, 1997; Gao et al., 1998; Pardoen and Delannay, 1998a,b). Only relatively crude, phenomenological void coalescence conditions were used to supplement the void growth models (as well as relatively crude void nucleation laws too, but this is outside the scope of the present paper). Typically, a constant critical value of the porosity is used as a material parameter, independent of the stress state, to indicate the onset of coalescence followed by a simple heuristic method to ramp down the stress to zero or to accelerate the damage evolution up to complete loss of the stress carrying capacity. These coalescence models involve thus at least two extra adjustable parameters.

In recent years, new efforts have been made to adapt or formulate better void coalescence conditions by introducing microstructural ingredients and micro-mechanical arguments (e.g., Zhang and Niemi (1995), Pardoen et al. (1998), Benzerga et al. (1999), Pardoen and Hutchinson (2000, 2003), Benzerga (2002), Benzerga et al. (2004a,b), based on the Thomason (1968, 1990) internal necking model), Benzerga et al. (1999) and Gologanu et al. (2001) introducing a two layers approach; Besson et al. (2003) addressing the problem of coalescence in shear; Perrin and Leblond (2000), Enakoutsa et al. (2005), Fabrègue and Pardoen (2008), introducing the effect of a second population) as well as new models for the final unloading process (Pardoen and Hutchinson, 2000, 2003; Benzerga, 2002; Benzerga et al., 2004b). On the one hand, the improvements made to the condition for the onset of void coalescence have already received several validations both from FE cell calculations or from comparison to experimental data (e.g., examples of assessments towards experimental data by Pardoen et al., 1998; Benzerga, 2000; Besson et al., 2003; Benzerga, 2004a,b; Ragab, 2004; Huber et al., 2005; Pardoen et al., 2003, 2004; Pardoen, 2006; Lassance et al., 2007; Weck et al., 2008). On the other hand, the models developed to predict the unloading rate during the coalescence stage from micromechanical arguments (Benzerga, 2000; Pardoen and Hutchinson, 2000, 2003; Benzerga, 2002; Benzerga et al., 2004b) have not received much attention in terms of critical assessment. Furthermore, the most advanced formulation involving a two yield-surface model proposed by Benzerga et al. (2000, 2004b) and Pardoen and Hutchinson (2003) involve some numerical difficulties when the system has to jump, at the onset of coalescence, from one yield surface to another consistently and it might be worth, with respect to large-scale structural simulations, considering more simple and numerically efficient heuristic

approaches, but with parameters motivated from micromechanical analysis. For instance, ramping down the stress to zero using simple numerical models, such as cohesive zone responses (e.g., Xia and Shih, 1995a,b, 1996; Ruggieri et al., 1996; Gao et al., 1998; Gullerud et al., 2000) or introducing an artificial acceleration of the rate of porosity growth without touching to the damage model formulation (Tvergaard and Needleman, 1984) probably remain attractive numerical strategies. But this does not preclude using physical arguments or other more advanced models to determine the parameters of such numerical models as already attempted by Benzerga (2002). Indeed, as shown in Pardoen and Hutchinson (2000) at moderate to high-stress triaxiality, an important part of the total energy associated to the damage process is spent during coalescence and attention must be given to accurately predict the end of the fracture process.

In this paper, we describe, assess and discuss a new simple model for predicting the strain increment (and thus the unloading rate) required to bring a material element being right at the onset of void coalescence up to final fracture. The model developed based on simple kinematics and geometric arguments is limited to void coalescence by internal necking. In its spirit, it follows earlier works by Benzerga (2002), though involving different assumptions and approximations, as well as a wider verification basis. This model can be connected to different existing void growth models, different criteria for the onset of void coalescence, and different numerical schemes for computing crack growth. It should ultimately enhance the predictive capabilities of full ductile fracture models, while decreasing by one the number of tuning parameters.

The paper starts by recalling some basics about void coalescence and by providing a short review of the literature about existing criteria for the onset of void coalescence and void coalescence models. The new model is described in section 'New Void Coalescence Model for Internal Necking' and verified in section 4 by comparison with finite element void cell simulations. The last conclusion section explains how this model can be incorporated into a full ductile fracture model.

VOID COALESCENCE: DESCRIPTION OF THE MECHANISMS AND EXISTING MODELS

Basics About Void Coalescence[1]

In ductile metals, the onset of void coalescence interrupts the mechanism of relatively homogenous void growth and constitutes the beginning of the

[1]Part of the material of this section is borrowed from Pardoen and Pineau (2007).

final stage of damage. In the most ductile metals, the void radius doubles or even triples with respect to its initial size, before coalescence sets in. In the less ductile metals, coalescence starts right after nucleation involving almost no void growth and the mechanism is said to be 'nucleation controlled' (see Worswick et al., 2001). The coalescence of voids consists of the transition from a stable phase of diffuse plastic deformation driving the stable growth of the voids to a localised mode of plastic deformation within the ligament separating two voids or a row of voids, with material off the localization plane usually undergoing elastic unloading. To establish precise terminology, 'void coalescence' is reserved for the part of the void enlargement evolution after the transition to the localized mode of plasticity, and 'void growth' is used to characterize void enlargement before localization. One must also distinguish the onset of void coalescence and the coalescence phase.

The first mode of coalescence, exhibited in the sequence (a–c) on Figure 1, is the *internal necking* mode of coalescence, where the ligament between the two voids shrinks with a shape typical of a necking process. Figure 1 (a–c) corresponds to SEM micrographs from Weck et al. (2008) obtained from 100 μm thick aluminium alloy sheets containing laser-drilled cylindrical holes and loaded in-situ in uniaxial tension. During the process of coalescence, the voids evolve towards a diamond shape. The fracture profile is macroscopically oriented at 90° with respect to the main loading direction. Another example of internal necking, now for initially rounded voids, is shown in Figure 1(e). This micrograph has been obtained from polished pre-strained steel samples (Benzerga, 2000).

The second mode of void coalescence shown in the sequence Figure 1(b–d) consists in a *shear localization* between large primary voids observed when the initial voids are distributed along lines at 45° from the main loading direction. This mode of coalescence is frequently observed in high-strength material with low or moderate strain hardening capacity. Another micrograph showing the shear localization mechanism is provided in Figure 1(f), again on prepared metallographic sections of pre-deformed samples. The micrograph shows inside the shear localization band the presence of secondary small voids. This mode of coalescence is frequently called '*void sheeting*'.

The third mode of void coalescence, called '*necklace coalescence*' (see Benzerga, 2000; Benzerga, 2004a) is less common. It has been observed to take place in rows of closely spaced voids gathering within elongated clusters. It consists of a localization process in a direction parallel to the main loading axis. An example is provided in Figure 1(g), with a column voids resulting from a long cluster of copper oxide particles within a copper matrix and giving rise to multiple void coalescence in a direction transverse to the main loading direction.

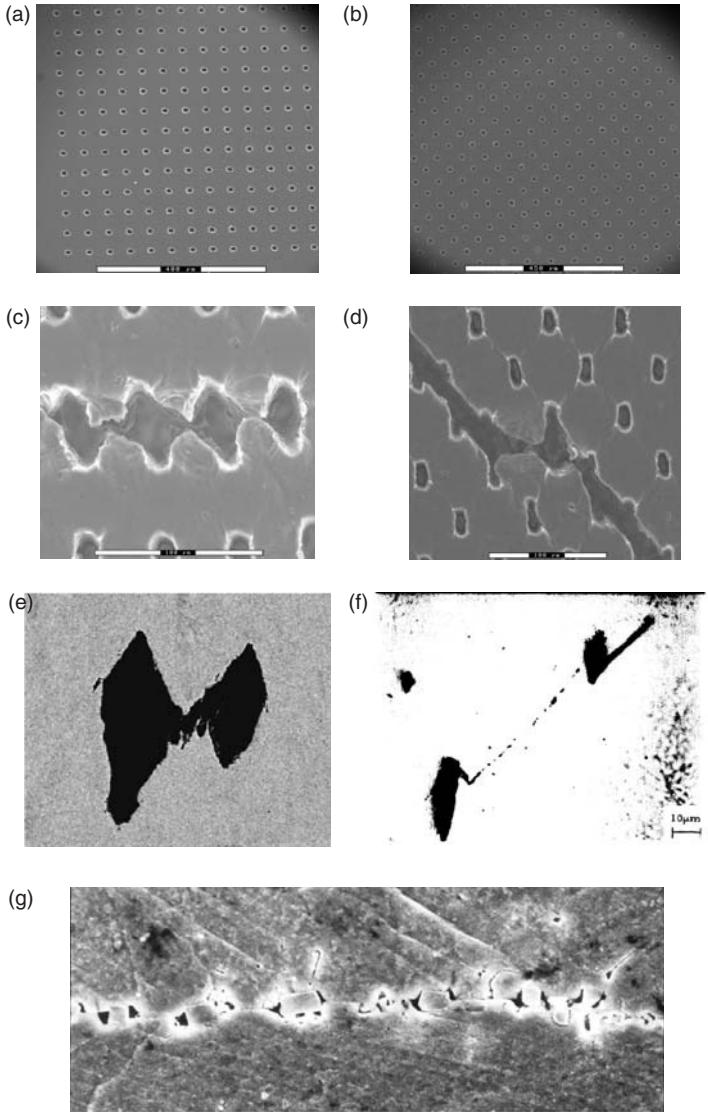

Figure 1. *Micrographs showing the different void coalescence mechanisms in metals. The loading direction is vertical except for figure (g); from (a) to (d) the experiments made on perforated aluminium sheets (courtesy of A. Weck and D.S. Wilkinson, see also Weck et al., 2008) with different arrangements of voids: arrangement (a) leads to internal necking (see (c)) and arrangement (b) leads to coalescence in shear (see (d)); micrograph (e) shows an internal necking process in steel (source, Benzerga, 2000); micrograph (f) shows a void sheet mechanisms in steel with many secondary voids along the microshear band (source, Cox and Low, 1974); micrograph (g) is an example of void coalescence in column or 'necklace', seen in extruded copper bars (source, Pardoen, 1998).*

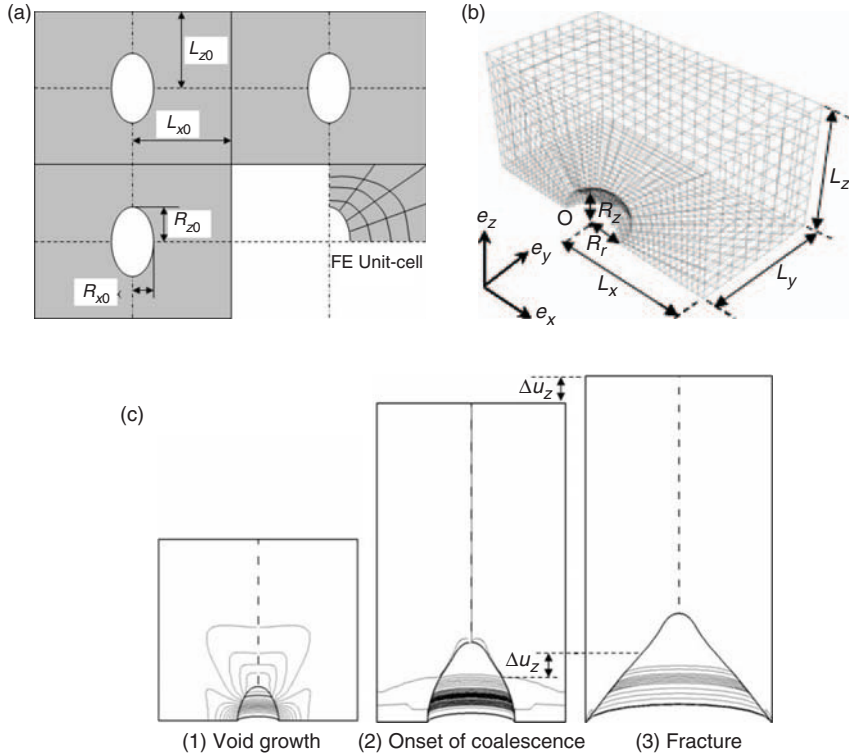

Figure 2. *Finite element unit cell calculations; (a) model material consisting of a periodic packing of unit cells involving one ellipsoidal void; (b) example of a 3D plane strain finite element cell; (c) evolution of the void morphology and $\dot{\varepsilon}^P_{zz}$ field in a cell subjected to a stress triaxiality $T=1$, (1) during void growth, (2) at the onset of coalescence, and (3) at final fracture (the void was initially spherical).*

Quantitative information about the void coalescence process can be gained from finite element unit cell calculations (Koplik and Needleman, 1988). As shown in Figure 2, the material is usually idealized by a periodic packing (although sometimes more complex representative volume elements are used, e.g., Thomson et al., 2003) of simple unit cells containing spheroidal voids of volume fraction f_0, aspect ratio $W_0 = R_{z0}/R_{x0}$, and anisotropy distribution parameter $\lambda_0 = L_{z0}/L_{x0}$ with the symmetry axis z oriented parallel to the main loading direction. The initial relative void spacing $\chi_0 = R_{x0}/L_{x0}$ is related to these three quantities through the following expression:

$$\chi_0 = \frac{R_{x0}}{L_{x0}} = \left(\frac{R^3_{x0}}{L^3_{x0}}\right)^{1/3} = \left(\frac{R^2_{x0}R_{z0}R_{x0}L_{z0}}{L^2_{x0}L_{z0}R_{z0}L_{x0}}\right)^{1/3} = \left(\frac{f_0}{\kappa}\frac{\lambda_0}{W_0}\right)^{1/3} \quad (1)$$

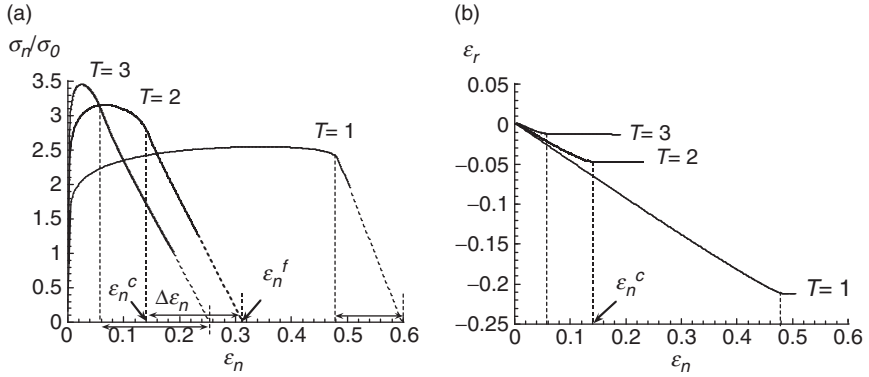

Figure 3. *Typical finite element void cell results: axisymmetric void cell simulations performed with the following set of parameters: $f_0 = 10^{-2}$, $\lambda_0 = 1$ and $W_0 = 1$, yield stress over Young's modulus ratio: $\sigma_0/E = 0.002$, strain hardening exponent: $n = 0.1$, under stress triaxiality: $T = 1$, 2, or 3; (a) variation of the axial stress as a function of the axial strain; (b) variation of the radial strain as a function of the axial strain. Definition of the strain at the onset of coalescence ε_n^c, final fracture strain ε_n^f and strain increment $\Delta\varepsilon_n$.*

where κ is a geometric factor which depends on the arrangement of voids (see e.g., Lassance et al., 2006; Pardoen and Pineau, 2007). Calculations can be performed in 2D or in 3D (an example of a 3D FE cell is shown in Figure 2(b)). Coalescence always occurs by internal necking when 2D axisymmetric conditions are used. Coalescence by internal necking is also observed in 3D cells when the strain hardening exponent is not too low, or when the stress triaxiality is moderate or high, or when the periodic void packing does not involve a closest neighbor near to 45° from the main loading direction (e.g., Richelsen and Tvergaard, 1994). The main characteristic of the internal necking mode is that it is a tensile mode of localization leading to a sharp transition into an uniaxial straining mode of the volume element imposed by the material outside the localization band which unloads elastically and behaves thus as a rigid block (see also Koplik and Needleman, 1988; Becker et al., 1989; Brocks et al., 1995; Richelsen and Tvergaard, 1994). The transition to an uniaxial straining mode is almost instantaneous (see also Koplik and Needleman, 1988, for initially oblate voids; Brocks et al., 1995; Richelsen and Tvergaard, 1994, for 3D computations). Figure 3 shows results from calculations performed on an axisymmetric void cell with $f_0 = 10^{-2}$, $W_0 = 1$, and $\lambda_0 = 1$, under constant stress triaxiality: $T = \Sigma_h/\Sigma_e = 1$, 2 or 3. The onset of coalescence is observed in the stress strain curve as a change of slope (a), but is more obvious when plotting, as in Figure 3(b), the variation of the radial strain ε_r as a function of the axial strain ε_z. Due to the transition to uniaxial straining, the rate of change of ε_r becomes suddenly almost equal to zero.

During coalescence, the stress drops linearly with increasing strain. This linearity has been verified by Tvergaard (1997) up to very large strains using remeshing techniques. Figure 3(a) also qualitatively exhibits the work spent during the void growth and coalescence processes from $\varepsilon_n = \varepsilon_{22} = 0$ to ε_n^c and from ε_n^c to ε_n^f, respectively (subscript/superscript 'c' refers to the onset of coalescence and 'f' to final fracture). The highest the stress triaxiality, the largest the relative importance of the coalescence process, with an energy dissipation of the same order of magnitude for the void growth and coalescence stages at $T = 2$.

Single void cell calculations, as experiments, also reveal the typical diamond shape of the void at the final fracture stage, as shown in Figure 2(c) which corresponds to a simulation made on a 3D unit cell (Figure 2(b)) with plane strain conditions imposed in the y direction. During coalescence, the radial growth of the void is significantly larger than the axial growth due to the lateral constraint resulting from the localization process and the shift to an uniaxial straining mode. The end of the coalescence process in a real material usually consists either, for the most ductile metals, in the radial growth up to final impingement, or in a premature failure of the remaining ligament (by microcleavage, crystallographic shearing, or with the help of a second population of smaller voids).

Models for the Onset of Void Coalescence

GENERIC PHENOMENOLOGICAL MODELS

(i) When using constitutive models coupling damage and plasticity, for instance the Gurson model (1977), there is a strain at which the overall stress reaches a maximum value. This maximum corresponds to the point where strain hardening does not compensate anymore for the damage induced softening. According to Mudry (1982), Koplik and Needleman (1988), or Becker (1987), fracture initiates rapidly after this maximum has been attained. This criterion based on attainment of a maximum effective stress is valid at low stress triaxiality, but not at large stress triaxiality, see Figure 3(a). (ii) The most widely employed criterion for the onset of void coalescence states that void coalescence starts at a critical porosity (McClintock, 1968a,b, 1971; d'Escatha and Devaux, 1979). Several numerical (e.g., Koplik and Needleman, 1988; Tvergaard, 1990; Brocks et al., 1995) and experimental/numerical works (e.g., Marini et al., 1985; Becker, 1987; Pardoen et al., 1998) have assessed the validity of this fracture criterion. For a well-defined material (and microstructure) and a limited range of stress states, this criterion is acceptable from a practical standpoint, especially in low porosity metallic alloys.

MICROMECHANICAL MODEL FOR VOID COALESCENCE BY INTERNAL NECKING

Different criteria have been proposed in the literature to predict the onset of void coalescence by internal necking following seminal ideas by Thomason (1968). (i) The criterion of Brown and Embury (1973) considers that in a perfectly plastic material, internal necking starts when it is possible for 45° micro-shear bands to connect two neighboring voids leading to an extremely simple, but robust, condition. (ii) A more advanced void coalescence model can be obtained by directly treating the mechanism of tensile plastic localization in the inter-void ligaments: diffuse plasticity throughout void containing cells gives way to localized deformation within the ligament with the material outside the ligament unloading elastically. An accurate analysis has been made by Thomason (1968,1990) who extensively studied the transition to localization for elastic-perfectly plastic solids using slip-line solutions leading to the following condition for the onset of void coalescence:[2]

$$\frac{\sigma_n}{\sigma_y}\frac{1}{(1-\chi^2)} = \alpha\left(\frac{1-\chi}{\chi W}\right)^2 + 1.24\sqrt{\frac{1}{\chi}} \tag{2}$$

where σ_y is the current mean yield stress of the matrix material surrounding the voids, the parameter α has been fitted as a function of the average value of the strain hardening exponent n: $\alpha(n) = 0.1 + 0.22n + 4.8n^2$ ($0 \le n \le 0.3$), see Pardoen and Hutchinson (2000). Criterion (2) states that coalescence occurs when the stress normal to the localization plane σ_n/σ_y reaches a critical value. This critical value decreases as the voids open (W increases) and get closer to each other (χ increases). The dominant parameter controlling the transition to the coalescence mode is the relative void spacing χ. The porosity affects the coalescence indirectly through the link with the void spacing χ and through its softening effect on the applied stress σ_z. In a more advanced application of this model (Scheyvaerts et al., 2009), the localization condition (2) is tested in all possible directions which requires to generalize the definition of χ and W as a function of the orientation of the localization plane. Recently, an extension of the condition (2) to the presence of a second population of voids has been proposed (Fabrégue and Pardoen, 2008).

[2]Note that some former references from our group (Huber et al., 2005; Lassance et al., 2006, 2007; Pardoen and Pineau 2007; Fabrégue and Pardoen, 2008) involved an erroneous multiplicative factor 2/3 in front of the right-hand side term of the Thomason model. This factor was not included in the code used to generate the results.

Models for the coalescence process

PHENOMENOLOGICAL ACCELERATION OF THE VOID GROWTH RATE

Tvergaard and Needleman (1984) have proposed to simulate the coalescence process by artificially accelerating the rate of increase of the true porosity f using an effective porosity f^* in the following way:

$$f^* = \begin{cases} f & \text{if } f < f_c \\ f_c + \delta(f - f_c) & \text{if } f \geq f_c \end{cases} \tag{3}$$

where f_c is the porosity at the onset of coalescence and the factor δ is an adjusting parameter, which varies between typically 3 and 8 and which can be fitted on void cell calculations or on experimental data. The idea is to preserve the format of the Gurson model after the onset of coalescence, which is numerically very convenient. Benzerga (2002) proposed, based on a theoretical analysis of the coalescence process (resembling the one addressed later in the core of this paper), a model to estimate δ.

NUMERICAL REDUCTION OF THE LOAD CARRYING CAPACITY

(i) Several authors (Xia et al., 1995) proposed, in the framework of a finite element implementation, to ramp down the stress in a given number of time increments after a critical porosity f_c is attained. There is no control on the energy dissipated during coalescence. (ii) A more advanced implementation has been developed by Shih, Dodds and co-workers (e.g., Xia and Shih, 1995a,b, 1996; Ruggieri et al., 1996; Gao et al., 1998; Gullerud et al., 2000). After the critical porosity is reached, a traction separation representation is used to ramp down the stress to zero. In this approach, the stress decreases with applied displacement and there is thus a control of the energy dissipated during coalescence. The adjusting parameter is the slope of the unloading ramp.

BILAYER MODEL

In the bilayer model proposed by Gologanu et al. (2001), each material element is made of a porous layer described by a Gurson type response and a nonporous layer. During deformation, the porosity grows in the porous layer up to a point where the induced softening overcome the strain hardening, and deformation starts localization in that layer. As a matter of fact, this model does not involve any coalescence criterion. Localization occurs naturally as well as the unloading response. Note that the specific evolution of the void morphology in the porous layer during coalescence is

not taken into account by the void growth model which is used indifferently before and during localization. The value of the parameter relating the relative portion of porous and nonporous zone must be prescribed.

FULL CONSTITUTIVE MODEL FOR THE INTERNAL NECKING PROCESS

As proposed by Benzerga (2000, 2002), Pardoen and Hutchinson (2003), and Benzerga et al. (2004b), the solution (2) is not only a condition for the onset of coalescence, but provides also the evolution of the stress during the full coalescence process as a function of the evolution of the shape and spacing of the voids. It constitutes thus the basis for elaborating a constitutive model for the full coalescence process. The solution (2) was transformed heuristically into a yield surface (Benzerga, 2000, 2002; Pardoen and Hutchinson, 2003; Benzerga et al., 2004b) and supplemented by the normality rule to evaluate the plastic strains. Evolution laws for the geometrical variables, i.e., the void aspect ratio, W, the porosity, f, and the relative void spacing χ, as well as for the current mean yield stress of the matrix material have been formulated based on simple geometrical rules. This coalescence model has been shown to capture quite well the drop of the load carrying capacity after the onset of coalescence (Pardoen and Hutchinson, 2000). However, numerical problems related to the jump from one yield surface to another make the implementation with robust finite element procedures more difficult than with other approaches.

NEW VOID COALESCENCE MODEL FOR INTERNAL NECKING

Physics of the Problem and Assumptions

The new model aims at describing the evolution of the void geometry from the point where plasticity localizes in the inter-void ligament to its final fracture. Most of the assumptions are motivated or guided by void cell simulation results.

The 1st assumption motivated by the mechanics of the localization process, clearly evidenced by the FE cell calculations (Figure 3(b)), consists of enforcing uniaxial straining during coalescence by imposing the transverse strain rates to be zero. The additional energy dissipation is then univocally determined by this unloading slope, i.e., by the normal displacement increment leading to final fracture, $\Delta\varepsilon_n$.

The shape of the zone in which plasticity localizes at the onset of coalescence is described schematically in Figure 4 for the case of an elongated void (a) (see also Figure 2(c)) and of a flat void (e). Figure 4(a) shows that the

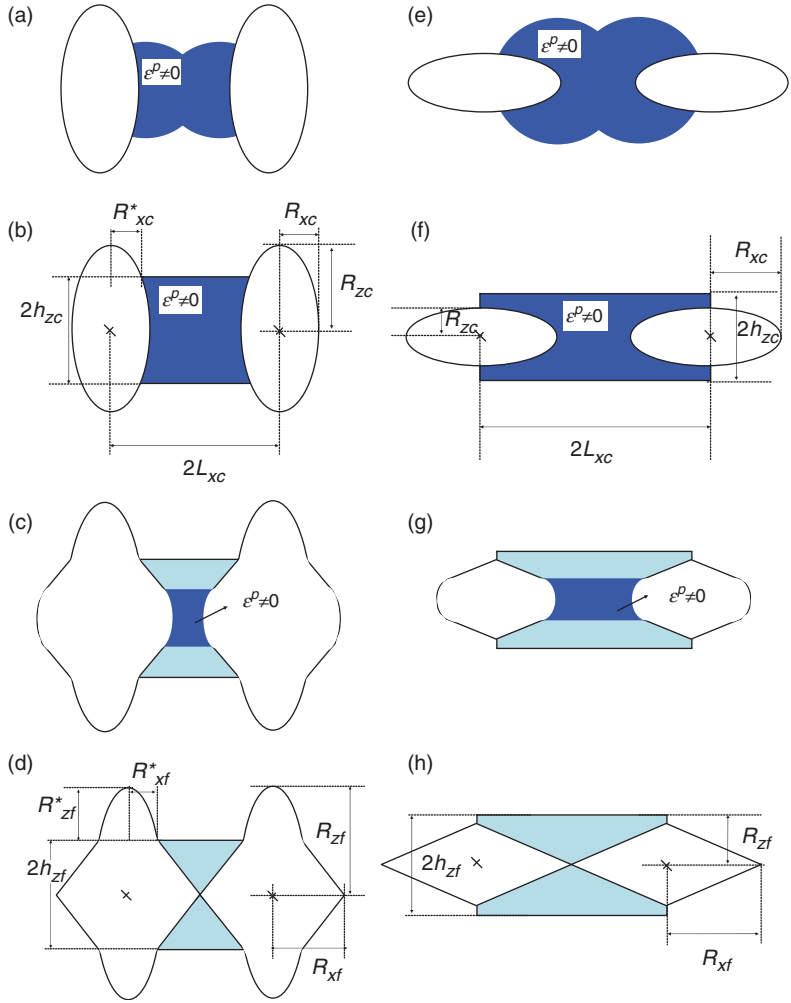

Figure 4. *Schematic evolution of the void and ligament geometry from, in (a) and (e), the onset of coalescence up to, in (d) and (h), final fracture; for (a) to (d) the localization zone height is only a fraction of the void radius R_{zc} ($\gamma_1 \leq 1 \gamma_1 < 1$); for (e) to (h) the localization zone height at the onset of coalescence, h_{zc}, encloses the cavity ($\gamma_1 \geq 1$); definition of the geometric parameter entering the coalescence model.*

height of the localization band can be much smaller than the void diameter $2R_z$ when the voids are very elongated at the onset of coalescence. Cell calculations always show that the opening of the void in the direction transverse to the ligament (i.e., the increase of R_z) is almost equal to the applied displacement on the cell after the onset of void coalescence whatever

the morphology of the void. This observation means that the pole of the cavity always sits in the elastic region as represented in Figure 4(a) and (e). Nevertheless, for the sake of simplicity, we will approximate (2nd assumption) the localization zone shape by a straight band, as depicted in Figure 4(b) and (f). The height of the band, noted $2h_{zc}$, which can be then smaller or larger than $2R_z$ depending on the void aspect ratio at the onset of coalescence, is the main unknown of the problem.

The 3rd assumption, motivated from both experimental observations as in Figure 1(c) and (e) and from void cell simulations as in Figure 2(c), is to consider that the void evolves towards a diamond shape, as represented in Figure 4(c, d) and (g, h). For each deformation increment, the internal necking progresses with an increment in the radial void growth, while a small outer layer previously in the active localization band starts unloading elastically. The size of the active plastic zone, i.e., the zone in which the plastic strain rate is different than zero, is thus decreasing with increasing reduction of the ligament, such as for a macroscopic neck in a tensile bar (e.g., Pardoen et al., 2004). By neglecting elastic strains, the displacement increment Δu_z applied to the cell can be considered to be entirely applied to the active localization band. Eventually, the ligament necks down to a point.

Hence, it is thus also tacitly assumed that the localization band keeps deforming as a band (the homogenous straining of the band is thus a 4th assumption) and fracture occurs by void impingement, neglecting possible accelerating factors such as the presence of a second population of voids or microcleavages taking place within the ligament (5th assumption). Finally, elastic strains are neglected (6th assumption). Three more assumptions will come later when developing the details of the model.

Model

HEIGHT OF THE LOCALIZATION BAND

At the onset of coalescence, plastic deformation is confined in a band of half length L_{xc} and half-height $h_{zc} = \gamma_1 R_{zc}$, with the parameter γ_1 yet unknown. The two options, $\gamma_1 < 1$ or $\gamma_1 \geq 1$ are depicted in Figure 4 (a)–(d) and (e)–(h), respectively. A different geometrical treatment is required for each case, as described in the next two sub-sections. Geometrical considerations motivate the assumption (7th assumption) that the height of the neck h_{zc} scales with the ligament length L_{xc}, while the scaling might depend on the strain hardening exponent (Pardoen et al., 2004), i.e., $\gamma_1 = h_{zc}/R_{zc} = g_1(n)(L_{xc}/R_{zc}) = g_1(n)(L_{xc}/R_{xc})(R_{xc}/R_{zc}) = g_1(n)(1/\chi_{xc}W_c)$, where the relative void spacing in the x direction $\chi_{xc} = R_{xc}/L_{xc}$ is introduced.

THE LOCALIZATION ZONE HEIGHT LARGER THAN THE VOID: $\gamma_1 \geq 1$

The volume of the localization band at the onset of coalescence V_c, i.e., the region undergoing plastic yielding, can be calculated based on the geometry given in Figure 4(f). Two different representative volume elements are considered here: (i) a cylinder subjected to axisymmetric loading conditions ($u_x = u_y = u_r$) and (ii) a parallepipedic unit-cell subjected to plane strain loading conditions ($u_y = 0$).

(i) For an axisymmetric RVE, the volume V_c^{AXI} is given by

$$V_c^{\mathrm{AXI}} = 2\pi L_{xc}^2 h_{zc} - \frac{4}{3}\pi R_{xc}^2 R_{zc} \quad (\gamma_1 \geq 1). \tag{4}$$

The height, at the end of the coalescence process, of the initial plastic localization band is equal to $h_{zf} = h_{zc} + \Delta u_z$ where Δu_z is the extra opening applied to the band from the onset of coalescence up to void impingement. The final void geometry is assumed to have the diamond double cone shape of half-height R_{zf} and radius R_{xf}, see Figure 4(h). The uniaxial straining constraint imposes that $R_{xf} \approx L_{xc}$. The final height of the void R_{zf} is not known and a geometric parameter γ_2 is introduced, defined by

$$\gamma_2 = \frac{R_{zf}}{R_{zc}}. \tag{5}$$

Based on the assumptions given above, γ_2 must be equal to $h_{zf}/R_{zc} = (h_{zc} + \Delta u_z)/R_{zc}$ at the transition between $\gamma_1 < 1$ and $\gamma_1 \geq 1$, i.e., when $\gamma_1 = 1$. At fracture, the volume corresponding to the material initially present in the localization band at the onset of coalescence is shown in Figure 4(h) and can be written as

$$V_f^{\mathrm{AXI}} = 2\pi L_{xc}^2 h_{zf} - \frac{2}{3}\pi L_{xc}^2 R_{zf} \quad (\gamma_1 \geq 1). \tag{6}$$

The additional normal strain increment associated to the displacement increment Δu_z can then be obtained by equating V_c^{AXI} and V_f^{AXI} (neglecting elastic deformations), which yields

$$\Delta\varepsilon_n^{\mathrm{AXI}} = \ln\left(1 + \frac{\Delta u_z}{L_{zc}}\right) = \ln\left(1 + \frac{\chi_{zc}}{3}\left[\gamma_2 - 2\chi_{xc}^2\right]\right) \quad (\gamma_1 \geq 1) \tag{7}$$

where $\chi_{zc} = R_{zc}/L_{zc}$ is the relative void spacing in the axial directions. The parameter γ_1 does not enter expression (7). The parameter γ_2 remains to be determined.

(ii) A similar approach can be followed for the plane strain case. At the onset of coalescence, the transverse cell dimensions are equal to L_{xc} and L_{y0} and the thickness of the localization band is equal to $\gamma_1 R_{zc}$. The corresponding material volume is given by

$$V_c^{PS} = 8L_{xc}L_{y0}h_{zc} - \frac{4}{3}\pi R_{xc}^2 R_{zc} \quad (\gamma_1 \geq 1). \tag{8}$$

At fracture, the cavity is a double cone of half-height R_{zf} given by (5), with a rectangular section of half-lengths L_{xc} and L_{y0}. The expression for the volume of material (8) in the final configuration then writes

$$V_f^{PS} = 8L_{xc}L_{y0}h_{zf} - \frac{2}{3}\pi L_{xc}R_{yf}R_{zf} \quad (\gamma_1 \geq 1). \tag{9}$$

By equating $V_c^{PS} = V_f^{PS}$, an expression for the strain increment is obtained

$$\Delta\varepsilon_n^{PS} = \ln\left(1 + \frac{\Delta u_z}{L_{zc}}\right) = \ln\left(1 + \frac{\pi}{12}\chi_{zc}\chi_{xc}\exp\left(\varepsilon_{tr}^c\right)\left[\frac{R_{yf}}{R_{xc}}\gamma_2 - 2\chi_{xc}\right]\right) \quad (\gamma_1 \geq 1), \tag{10}$$

where the deformation in the in-plane transverse direction at the onset of coalescence ε_{tr}^c is defined as $\varepsilon_{tr}^c = \ln(L_{xc}/L_{x0})$ from which one gets $R_{xc}/L_{y0} = \chi_{xc}\exp\left(\varepsilon_{tr}^c\right)$. Based on an analysis of FE cell calculations, a simple correction is introduced for the difference between the growth of the void in the x and y directions during coalescence: $R_{yf}/R_{xc} = \left(2 - \exp\left(\varepsilon_{tr}^c\right)\right)/\chi_{xc}$ (note that $R_{yf} = R_{xf}$ when $L_{y0} = L_{xc}$). A more accurate correction can be found in Scheyvaerts et al. (2009). The axisymmetric and plane strain models are thus compatible, allowing future extension to general loading conditions. Again, the parameter γ_2 remains to be determined.

THE LOCALIZATION ZONE HEIGHT IS CONFINED IN THE LIGAMENT: $\gamma_1 < 1$

For ligament a half-height smaller than R_{zc}, the material volume undergoing plastic deformation at the onset of coalescence, V_c, is shown in Figure 4(b). The radius of the section of the void at a height h_{zc} is noted R_{xc}^*.

(i) Based on the relationship $R_{xc}^{*2} = \left(1 - \gamma_1^2\right)R_{xc}^2$, the volume V_c for an axisymmetric RVE writes

$$V_c^{\mathrm{AXI}} = 2\pi L_{xc}^2 h_{zc} - \frac{2}{3}\pi R_{xc}^2 R_{zc}\left(3\gamma_1 - \gamma_1^3\right) \quad (\gamma_1 < 1). \tag{11}$$

As before, the ligament half-height at fracture is given by $h_{zf} = h_{zc} + \Delta u_z$. Because the material outside the ligament region is elastic, it can be

considered that R^*_{xc} does not evolve during coalescence and thus $R^*_{xf} = R^*_{xc}$. The final void geometry for an axisymmetric RVE is assumed to have a double truncated cone shape of base radius L_{xc} without the upper part of base radius R^*_{xf}, see Figure 4(h). Using elementary geometrical rules, the volume of the localization band at fracture can be expressed as

$$V_f^{\mathrm{AXI}} = 2\pi L_{xc}^2 h_{zf} - \frac{2}{3}\pi h_{zf}\left[R_{xc}^{*2} + \left(L_{xc}^2 - R_{xc}^* 2\right)\frac{L_{xc}}{L_{xc} - R_{xc}^*}\right] \quad (\gamma_1 < 1). \tag{12}$$

By equating the two volumes, the additional normal strain increment can be isolated as

$$\begin{aligned}\Delta\varepsilon_n^{\mathrm{AXI}} &= \ln\left(1 + \frac{\Delta u_z}{L_{zc}}\right) \\ &= \ln\left(1 + \gamma_1\chi_{zc}\left[\frac{1 + \chi_{xc}\sqrt{1-\gamma_1^2} - 2\chi_{xc}^2}{2 + \left(\gamma_1^2 - 1\right)\chi_{xc}^2 - \sqrt{1-\gamma_1^2}\chi_{xc}}\right]\right) \quad (\gamma_1 < 1),\end{aligned} \tag{13}$$

which is independent of γ_2. No hypothesis on the final void height (similar to (5)) is necessary in this configuration, since the top of the void lies outside the volume under consideration. Hence, γ_2 does not enter Equation (13). An expression for $\gamma_1 = g_1(n)(1/\chi_{xc}W_c)$ remains to be determined.

(ii) A similar approach can be followed for the plane strain case. At the onset of coalescence, the transverse dimensions of the localization zone are equal to L_{xc} and L_{y0} and the thickness is equal to $\gamma_1 R_{zc}$. The corresponding material volume writes

$$V_c^{PS} = 8L_{xc}L_{y0}h_{zc} - \frac{2}{3}\pi R_{xc}^2 R_{zc}\left(3\gamma_1 - \gamma_1^3\right) \quad (\gamma_1 < 1) \tag{14}$$

while this material volume becomes a double cone without its extremities in the final configuration, given by

$$V_f^{PS} = 8L_{xc}L_{y0}h_{zf} - \frac{2}{3}\pi h_{zf}\left[R_{xc}^{*2} + \left(L_{xc}R_{yf} - R_{xc}^* 2\right)\frac{L_{xc}}{L_{xc} - R_{xc}^*}\right] \quad (\gamma_1 < 1). \tag{15}$$

By equating $V_c^{PS} = V_f^{PS}$, the expression for the strain increment writes, after elementary algebra

$$\Delta\varepsilon_n^{PS} = \ln\left(1 + \gamma_1\chi_{zc}\left[\frac{\chi_{xc}^2\exp\left(\varepsilon_{tr}^c\right)\left(3 - \gamma_1^2\right) - A}{A - (12/\pi)}\right]\right) \quad (\gamma_1 < 1). \tag{16}$$

with

$$A = \chi_{xc} \exp\left(\varepsilon_{tr}^{c}\right) \left[\frac{\left(R_{yf}/R_{xc}\right) - \chi_{xc}^{2}\left(1-\gamma_1^2\right)^{3/2}}{1 - \chi_{xc}\sqrt{1-\gamma_1^2}} \right]. \tag{17}$$

As above, one considers that $R_{yf}/R_{xc} = \left(2 - \exp\left(\varepsilon_{tr}^{c}\right)\right)/\chi_{xc}$. In order to provide a predictive model for the normal strain increment during the final necking process, an expression for $\gamma_1 = g_1(n)(1/\chi_{xc}W_c)$ remains to be specified.

Determination of the Shape Parameters γ_1 and γ_2

A large set of FE cell calculations has been used to determine expressions for the unknown shape parameters $\gamma_1 = g_1(n)(1/\chi_{xc}W_c)$ and γ_2 that minimize the error on the predicted $\Delta\varepsilon_n$. Note also that the two parts of the model have been set to converge to the same prediction for $\gamma_1 = 1$. The following methodology was followed. Both γ_1 and γ_2 can be expressed as a function of $\Delta\varepsilon_n$, ε_{tr}^{c}, χ_{zc}, and χ_{xc} using Equations (7) and (10), and (13) and (16), respectively. Each FE cell calculation provides a set of values for $\Delta\varepsilon_n$,ε_{tr}^{c}, χ_{zc}, and χ_{xc}, from which γ_1 and γ_2 can thus be inferred. At this stage, it is not known whether γ_1 will be higher or smaller than 1, and it is thus evaluated for all data available. (Note that some data, which turned out later to belong to the range $\gamma_1>1$, lead to no solution to the equation of the 6th or 8th order resulting from (13) or (16), respectively). Repeating this procedure for each cell calculation generates a large data bank of γ_1 and γ_2 corresponding to a different set of conditions (initial void shape, initial void volume fraction, stress triaxiality, strain hardening exponent) on which the minimization can be performed.

More precisely, use will be made here of both 2D axisymmetric and 3D FE void cells calculations performed with the general purpose FE software Abaqus (Abaqus, 2004). The axisymmetric cell calculations have already been presented earlier (Pardoen and Hutchinson, 2000; Lassance et al., 2006). The 3D cell calculations are new and have been performed under plane strain conditions in the y direction, while assuming periodic boundary conditions in the x and z directions. Constant stress triaxiality is enforced by an iterative scheme as described in Pardoen and Hutchinson, 2000. The finite element mesh used for the 3D calculations is shown in Figure 2(b). A J_2 isotropic hardening elastic-plastic response is assumed for the matrix, characterized by the following representation in uniaxial tension

$$\frac{\sigma}{\sigma_0} = \frac{E}{\sigma_0}\varepsilon \qquad \text{for } \sigma < \sigma_0, \tag{18}$$

$$\frac{\sigma}{\sigma_0} = \left(1 + \frac{E}{\sigma_0}\varepsilon^{p}\right)^{n} \qquad \text{for } \sigma > \sigma_0, \tag{19}$$

where E is the Young's modulus, σ_0 is the initial yield stress, and n is the strain hardening exponent. The Poisson ratio of the matrix ν is always taken equal to 0.3.

A wide range of parameters has been tested with W_0 varying between 10^{-3} (very flat) and 6, f_0 varying between 10^{-5} and 10^{-1}, λ_0 varying between 1 and 4, T varying between 1/3 and 3 and n equal to 0.1 and 0.3. The onset of coalescence was detected from the sudden change in the evolution of the transverse strain rate, see Figure 3(b). At high stress triaxiality and for highly elongated cells ($\lambda >> 1$), the transition is not so marked due to elastic effects and there might be a small source of error in the definition of the exact onset. The strain increment $\Delta\varepsilon_n$ is obtained by extrapolating the linear unloading curve down to zero, see Figure 3(a). Consequently, the accuracy of the $\Delta\varepsilon_n$ values extracted from the cell calculations depends on when the calculations are stopped after the onset of coalescence due to convergence problems and on the accuracy of the FE model, related to the degree of mesh distortion attained next to the void surface where the deformation is the most intense. The presence of this source of error in the present assessment is compensated by working with a large set of results. The subscript/superscript '*0*' corresponds to initial conditions, '*c*' to the onset of coalescence, and '*f*' to final fracture. In the axisymmetric cases, the yield stress σ_0/E is equal to 0.002. The results of these calculations are reported in Table 1 for $n = 0.1$ and Table 2 for $n = 0.3$. The results obtained with the 3D plane strain cell calculations concern materials with $\sigma_0/E = 0.003$, $n = 0.1$ and are given in Table 3. The values of the parameters at the onset of coalescence are also indicated in Tables 1–3.

The analysis of the results shows that the form of the function chosen for γ_1, i.e., $\gamma_1 = g_1(n)(1/\chi_{xc}W_c)$, motivated by geometrical considerations about the necking zone, is indeed capturing all the first-order effects. Using more complex functions does not improve significantly the quality of the fitting. The best fit is obtained with $g_1(n = 0.1) = 0.5$ for $n = 0.1$ (when combining axisymmetric and plane strain data) and $g_1(n = 0.3) = 0.3$ for $n = 0.3$. The error coming from neglecting the effect of the strain hardening exponent n being very small, a constant value $g_1 = 0.5$ is used, hence

$$\gamma_1 = \frac{0.5}{\chi_{xc}W_c} \tag{20}$$

has thus been chosen for the sake of simplicity.

Geometric considerations motivate the assumption (8th assumption) that γ_2 is primarily related to χ_{xc}, hence $\gamma_2 = g_2(n,\chi_{xc})$. Figure 5 shows the

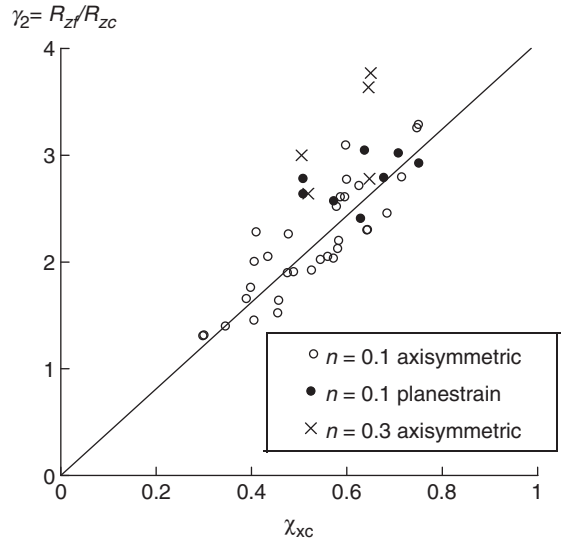

Figure 5. *Variation of the parameter $\gamma_2 = R_{zf}/R_{zc}$ as a function of χ_{xc}; γ_2 is calculated based on solving Equations (7) and (10), using the fracture strains obtained with the FE cell calculations.*

variation of γ_2 as a function of χ_{xc} for all the results belonging to $\gamma_1 > 1$. The linear fit

$$\gamma_2 = \frac{R_{zf}}{R_{zc}} = 4\chi_{xc} \tag{21}$$

with no dependence on the strain hardening is sufficiently accurate for the sake of the present model.

Summary – Closed form Expressions for the Coalescence Stage

Based on expressions (20) and (21), analytical expressions for the strain increment corresponding to the coalescence stage can be given, as summarized in Table 4, assuming that the quantities $\left(W_c, \chi_{xc}, \chi_{zc}, \varepsilon_{tr}^c\right)$ are known at the onset of coalescence (from void cell calculations or from a suitable void growth model supplemented by a void nucleation law, see section 'Discussion and Conclusion'). By assuming (9th assumption) that the stress normal to the ligament decreases linearly with additional straining during coalescence, consistent with the unit-cell results gathered in Figure 3(a) (see also Tvergaard, 1997) and knowing the overall maximum principal stress at the onset of coalescence Σ_c, one can directly estimate the unloading slope as $\Sigma_c/\Delta E_n$.

ASSESSMENT

The predictions made with the equations of Table 4 for $\Delta\varepsilon_n$ are now compared to the finite element void cell results. This is not a true verification of the model because the same data have been used to identify the parameters γ_1 and γ_2, but an assessment of the accuracy of the model within a very broad range of conditions. Figure 6(a)–(c) shows the relative error made on the predicted $\Delta\varepsilon_n$, i.e., $\Delta\varepsilon_n^{\text{FEcell}} - \Delta\varepsilon_n^{\text{model}} / \Delta\varepsilon_n^{\text{FEcell}}$, as a function of the void aspect ratio at the onset of void coalescence W_c, for all the

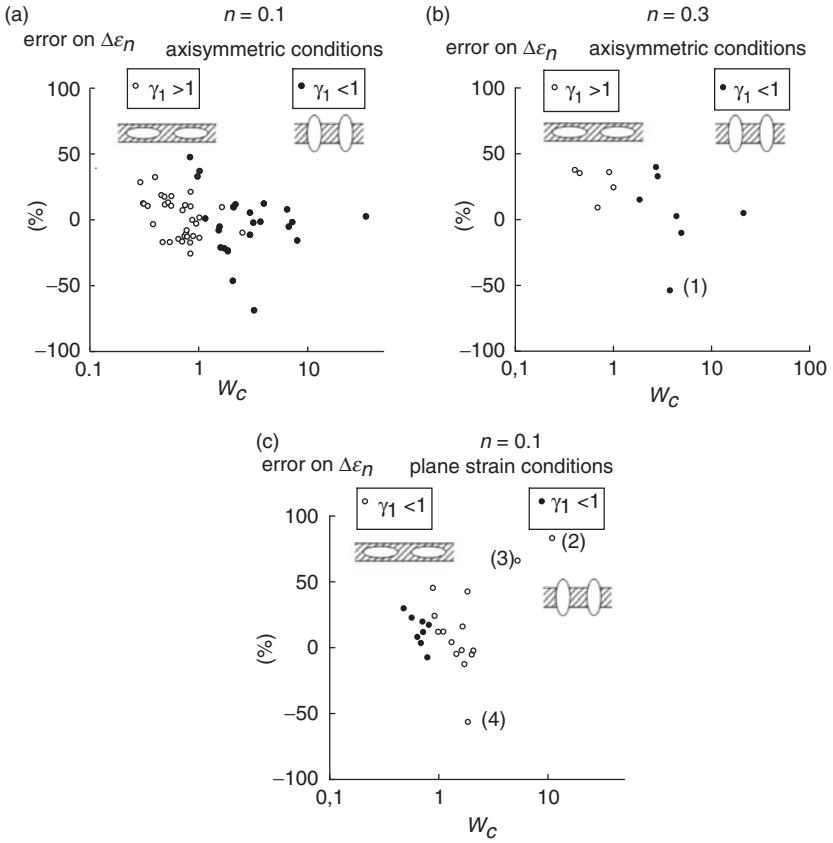

Figure 6. *Relative error made on the predicted additional strain increment from onset of coalescence until final fracture as a function of the void aspect ratio at the onset of coalescence w_c for (a) axisymmetric loading conditions with $n = 0.1$, (b) axisymmetric loading conditions with $n = 0.3$, and (c) plane strain loading conditions with $n = 0.1$; for many different initial void volume fraction f_0, initial void shape W_0, initial distribution parameter λ_0, stress triaxiality T.*

conditions gathered in Tables 1–3. First of all, it is interesting to note that the transition between $\gamma_1 < 1$ and $\gamma_1 \geq 1$ takes place around $W_c = 1$. Furthermore, it was also verified that the two parts of the model for $\gamma_1 < 1$ and $\gamma_1 \geq 1$ converge towards the same values for $\gamma_1 = 1$, i.e., γ_2 tends towards $h_{zf}/R_{zc} = (h_{zc} + \Delta u_z)/R_{zc}$ at $\gamma_1 = 1$.

Table 1. Results of axisymmetric finite element void cell calculations (59 cases), corresponding to $\sigma_0/E = 0.002$, $n = 0.1$, various initial void volume fractions f_0, initial void shapes W_0, initial distribution parameters λ_0, and stress triaxialities T; values of the geometrical parameters at the onset of coalescence f_c, W_c, λ_c, χ_c, $R_z/L_z|_c$, strain at the onset of void coalescence ε_n^c and at final fracture ε_n^f.

f_0 (%)	W_0	λ_0	T	f_c (%)	W_c	λ_c	χ_c	$R_z/L_z\|_c$	ε_n^c	ε_n^f	Data from
0.01	1/6	1	1	1.61	1.42	3.66	0.40	0.15	0.87	–	PH
0.01	1/6	1	2	2.10	0.52	1.46	0.45	0.16	0.26	–	PH
0.01	1/6	1	3	2.62	0.56	1.17	0.43	0.21	0.11	0.22	PH
0.01	1	1	1	1.52	2.05	6.02	0.41	0.14	1.20	1.24	PH
0.01	1	1	3/2	2.35	0.84	2.25	0.45	0.17	0.55	0.61	PH
0.01	1	1	2	2.62	0.65	1.58	0.46	0.19	0.32	0.39	PH
0.01	1	1	3	2.37	0.71	1.18	0.39	0.23	0.12	0.22	PH
0.01	6	1	1	1.54	8.00	13.1	0.34	0.20	1.72	1.74	PH
0.01	6	1	2	2.76	1.01	1.60	0.40	0.26	0.32	0.41	PH
0.01	6	1	3	2.39	1.01	1.16	0.34	0.30	0.11	0.22	PH
1	1/6	1	1/3	7.86	3.16	5.75	0.60	0.33	1.19	1.25	PH
1	1/6	1	2/3	7.68	0.83	1.89	0.64	0.28	0.45	0.56	PH
1	1/6	1	1	6.58	0.54	1.47	0.64	0.24	0.28	0.39	PH
1	1/6	1	2	4.79	0.34	1.17	0.62	0.18	0.12	0.23	PH
1	1/6	1	3	3.75	0.29	1.09	0.60	0.16	0.07	0.18	PH
1	1	1	2/3	6.40	3.67	4.48	0.49	0.40	1.02	1.10	PH
1	1	1	1	6.19	1.55	2.00	0.49	0.38	0.48	0.61	PH
1	1	1	1.65	5.60	0.95	1.32	0.49	0.35	0.20	0.36	PH
1	1	1	2	5.16	0.87	1.21	0.47	0.34	0.14	0.29	PH
1	1	1	3	3.51	0.84	1.07	0.41	0.32	0.06	0.22	PH
1	6	1	2/3	10.5	34.2	19.7	0.45	0.78	2.02	2.04	PH
1	6	1	1	9.00	6.47	3.30	0.41	0.80	0.82	0.94	PH
1	6	1	2	6.06	2.95	1.23	0.34	0.81	0.16	0.39	PH
1	6	1	3	3.63	3.21	1.06	0.26	0.79	0.05	0.32	PH
0.1	1	1	1	3.05	1.84	3.41	0.44	0.24	0.85	0.92	PH
0.1	1	2	1	1.73	1.71	5.33	0.43	0.14	0.67	–	PH
0.1	1	4	1	1.01	1.59	8.61	0.43	0.08	0.51	0.54	PH
0.0625	1/6	1	1	4.27	0.97	2.36	0.54	0.22	0.59	0.68	PH
0.0625	1/6	2	1	2.25	0.76	3.65	0.54	0.11	0.41	0.46	PH
0.0625	1/6	1	3	2.90	0.45	1.13	0.48	0.19	0.10	0.20	PH
0.0625	1/6	2	3	0.89	0.40	2.05	0.41	0.08	0.03	0.08	PH
0.0625	1	1	1	3.05	1.84	3.41	0.44	0.24	0.83	0.90	PH

(*continued*)

Table 1. Continued.

f_0 (%)	W_0	λ_0	T	f_c (%)	W_c	λ_c	χ_c	$R_z/L_z\|_c$	ε_n^c	ε_n^f	Data from
0.0625	1	2	1	1.73	1.71	5.33	0.43	0.14	0.66	0.70	PH
0.0625	1	1	3	2.77	0.75	1.13	0.40	0.26	0.10	0.21	PH
0.0625	1	2	3	0.71	0.84	2.10	0.30	0.12	0.04	0.08	PH
0.0625	6	1	1	3.52	7.20	6.24	0.36	0.41	1.23	1.29	PH
0.0625	6	2	1	2.13	6.70	8.97	0.35	0.26	1.01	1.05	PH
0.0625	6	1	3	2.65	1.63	1.11	0.30	0.44	0.08	0.23	PH
0.0625	6	2	3	0.74	2.51	2.08	0.21	0.25	0.03	0.09	PH
1	0.1	1	1	6.88	0.38	1.34	0.71	0.20	0.22	0.33	LD
1	1	1	2/3	6.54	3.95	4.89	0.49	0.40	1.08	1.16	LD
1	1	1	1	6.32	1.53	1.98	0.50	0.38	0.48	0.60	LD
1	1	1	3/2	5.78	1.02	1.40	0.49	0.36	0.24	0.39	LD
0.5	0.5	1	2/3	5.28	2.96	4.80	0.50	0.31	1.06	1.14	LD
0.5	0.5	1	1	5.28	1.15	2.06	0.52	0.29	0.50	0.60	LD
0.5	0.5	1	3/2	4.87	0.74	1.48	0.53	0.26	0.28	0.39	LD
0.2	0.2	1	1	4.90	0.89	2.12	0.56	0.23	0.52	0.62	LD
0.2	0.2	1	3/2	4.68	0.56	1.54	0.58	0.21	0.30	0.42	LD
0.1	0.01	1	1	6.38	0.31	1.36	0.75	0.17	0.23	0.34	LD
0.1	0.1	1	2/3	4.54	2.17	4.66	0.53	0.25	1.04	1.12	LD
0.1	0.1	1	1	4.82	0.83	2.15	0.57	0.22	0.53	0.62	LD
0.1	0.1	1	3/2	4.51	0.52	1.55	0.59	0.20	0.31	0.43	LD
0.01	0.001	1	1	6.34	0.31	1.36	0.75	0.17	0.23	0.34	LD
0.01	0.01	1	2/3	4.59	2.09	4.75	0.54	0.24	1.05	1.13	LD
0.01	0.01	1	1	4.69	0.78	2.17	0.58	0.21	0.53	0.63	LD
0.01	0.01	1	3/2	4.36	0.49	1.57	0.59	0.18	0.32	0.43	LD
0.001	0.001	1	2/3	4.69	2.07	4.77	0.55	0.24	1.06	1.14	LD
0.001	0.001	1	1	4.68	0.77	2.18	0.58	0.21	0.53	0.63	LD
0.001	0.001	1	3/2	4.40	0.48	1.58	0.60	0.18	0.32	0.44	LD
2	0.2	1	1	7.53	0.46	1.32	0.68	0.24	0.20	0.32	LD
5	0.5	1	1	9.94	0.70	1.25	0.64	0.36	0.17	0.33	LD
10	1	1	1	14.7	1.09	1.17	0.62	0.58	0.12	0.37	LD

The data are collected from Pardoen and Hutchinson (2000) (PH) and from Lassance et al. (2006) (LD). Subscript/superscript '0' corresponds to initial conditions, '*c*' to the onset of coalescence, and '*f*' to final fracture.

Among the 94 cases, only 4 predictions produce an error larger than 50%. These cases correspond to

(1) $n=0.3$, $f_0=10^{-2}$, $W_0=1/6$, $\lambda_0=1$, $T=1/3$, $\varepsilon_n^c=1.19$ and $\varepsilon_n^f=1.25$ (Figure 6(b) and Table 2)
(2) $n=0.1$, $f_0=10^{-2}$, $W_0=1$, $\lambda_0=1$, $T=0.58$, $\varepsilon_n^c=1.51$ and $\varepsilon_n^f=1.73$ (Figure 6(c) and Table 3)
(3) $n=0.1$, $f_0=10^{-3}$, $W_0=6$, $\lambda_0=1$, $T=1$, $\varepsilon_n^c=1.08$ and $\varepsilon_n^f=1.27$ (Figure 6(c) and Table 3)
(4) $n=0.1$, $f_0=2\times10^{-2}$, $W_0=1$, $\lambda_0=1/2$, $T=1$, $\varepsilon_n^c=0.75$ and $\varepsilon_n^f=1.02$ (Figure 6(c) and Table 3)

Table 2. Results of axisymmetric finite element void cell calculations (12 cases), corresponding to $\sigma_0/E = 0.002$, $n = 0.3$, various initial void volume fractions f_0, initial void shapes W_0, initial distribution parameters λ_0, and stress triaxialities T; values of the geometrical parameters at the onset of coalescence f_c, W_c, λ_c, χ_c, $R_z/L_z|_c$, strain at the onset of void coalescence ε_n^c and at final fracture ε_n^f.

f_0 (%)	W_0	λ_0	T	f_c (%)	W_c	λ_c	χ_c	$R_z/L_z\|_c$	ε_n^c	ε_n^f	Data from
1	1/6	1	1/3	7.04	3.77	7.23	0.59	0.31	1.34	1.38	PH
1	1/6	1	1	7.54	0.69	1.65	0.65	0.27	0.36	0.52	PH
1	1/6	1	2	6.48	0.45	1.25	0.64	0.23	0.17	0.37	PH
1	1/6	1	3	6.39	0.40	1.16	0.65	0.23	0.12	0.32	PH
1	1	1	2/3	6.47	4.38	5.45	0.49	0.40	1.15	1.23	PH
1	1	1	1	6.74	1.85	2.34	0.50	0.40	0.59	0.75	PH
1	1	1	2	6.97	1.00	1.34	0.52	0.39	0.22	0.46	PH
1	1	1	3	6.66	0.91	1.17	0.50	0.39	0.13	0.41	PH
1	6	1	2/3	12.0	21.1	22.0	0.57	0.55	2.10	2.12	PH
1	6	1	1	12.5	4.92	3.75	0.52	0.69	0.9	0.99	PH
1	6	1	2	8.54	2.82	1.38	0.40	0.81	0.24	0.59	PH
1	6	1	3	6.58	2.72	1.14	0.35	0.82	0.11	0.54	PH

The data are collected from Pardoen and Hutchinson (2000) (PH). Subscript/superscript '0' corresponds to initial conditions, '*c*' to the onset of coalescence, and '*f*' to final fracture.

Care must be taken when analyzing this seemingly poor agreement between the model and the cell calculations for these four cases. First of all, all these results belong to either one axisymmetric cases with $n = 0.3$ or to plane strain cases. The search for a good fit for the parameter γ_1 and γ_2 was dominated by the large number of axisymmetric results with $n = 0.1$. A more honestly balanced fit among the three different conditions ($n = 0.1$ – axisymetric, $n = 0.3$ axisymmetric, $n = 0.1$ plane strain) could improve the predictions for the worst cases (1)–(4) (and some others). Furthermore, an effect of n could be introduced to improve the predictions for $n = 0.3$, but at the expense of simplicity (the extension of a necking region is indeed known to depend on strain hardening, see Pardoen et al., 2004; Pardoen, 2006). Note that for the plane strain conditions, one could refine the expression relating the two in plane radius R_y and R_x, which might be a necessary step required to build a generalized version of the model. Finally, it should be remembered, as explained in section 'Determination of the Shape Parameters γ_1 and γ_2', that the fracture strain ε_n^f is never attained in the FE cell calculations, but obtained by extrapolation of the results. The accuracy of this extrapolation varies from one simulation to another, depending, among others, on when the simulation is interrupted due to heavy mesh distortions. The worst cases (1)–(4) discussed here belong to cell calculations associated to large fracture strains, thus involving very large local strains

Table 3. Results of plane strain finite element void cell calculations (23 cases), corresponding to $\sigma_0/E = 0.003$, $n = 0.1$, various initial void volume fractions f_0, initial void shapes W_0, initial distribution parameters λ_0, and stress triaxialities T; values of the geometrical parameters at the onset of coalescence $f_c, W_c, \lambda_c, \chi_c, R_z/L_z|_c$, strain at the onset of void coalescence ε_n^c and at final fracture ε_n^f.

f_0 (%)	W_0	λ_0	T	f_c (%)	W_c	λ_c	χ_c	$R_z/L_z\|_c$	ε_n^c	ε_n^f	Data from
0.01	1	1	1.5	4.12	0.86	3.28	0.66	0.24	0.62	0.75	FS
0.01	1	1	2	3.93	0.67	1.84	0.59	0.25	0.33	0.46	FS
0.01	1	1	3	4.09	0.64	1.24	0.54	0.30	0.13	0.28	FS
0.1	1/6	1	1	7.05	1.07	3.64	0.72	0.31	0.68	0.85	FS
0.1	1/6	1	1.5	6.09	0.65	1.95	0.68	0.28	0.37	0.54	FS
0.1	1/6	1	2	6.06	0.52	1.50	0.68	0.27	0.24	0.42	FS
0.1	1/6	1	3	5.15	0.46	1.19	0.63	0.25	0.12	0.30	FS
0.1	1	1	1	5.44	1.73	5.52	0.65	0.31	0.88	1.02	FS
0.1	1	1	1.5	5.36	0.92	2.25	0.62	0.31	0.44	0.56	FS
0.1	1	1	2	5.28	0.76	1.57	0.59	0.31	0.26	0.40	FS
0.1	1	1	3	4.13	0.72	1.18	0.50	0.30	0.11	0.27	FS
0.1	6	1	1	5.75	4.31	8.06	0.55	0.50	1.08	1.27	FS
0.1	6	1	1.5	5.70	1.97	2.45	0.51	0.52	0.48	0.63	FS
0.1	6	1	2	4.96	1.63	1.56	0.45	0.53	0.25	0.43	FS
0.1	6	1	3	3.88	1.47	1.15	0.39	0.52	0.10	0.28	FS
1.0	1	1	0.577	9.25	5.36	18.5	0.67	0.48	1.51	1.73	FS
1.0	1	1	1	9.16	1.48	2.70	0.65	0.47	0.54	0.71	FS
1.0	1	1	1.5	7.66	1.02	1.60	0.60	0.43	0.27	0.45	FS
1.0	1	1	2	7.44	0.83	1.32	0.60	0.40	0.18	0.35	FS
1.0	1	1	3	5.01	0.80	1.11	0.51	0.37	0.08	0.26	FS
0.25	1	4	1	2.73	1.57	10.3	0.66	0.13	0.49	0.58	FS
0.5	1	2	1	4.47	1.44	4.78	0.63	0.24	0.46	0.57	FS
2.0	1	0.5	1	18.1	1.52	1.87	0.70	0.81	0.75	1.02	FS

The data are collected from Scheyvaerts et al. (2009) (FS). Subscript/superscript '0' corresponds to initial conditions, '*c*' to the onset of coalescence, and '*f*' to final fracture.

and large mesh distortions already at the onset of coalescence. The accuracy of the $\Delta\varepsilon_n$ values extracted from the FE cell calculations is not guaranteed. Hence, as a first methodological conclusion, if there is indeed room for extension and improvement of this model, these efforts should ideally be undertaken based on very robust FE cell calculations, involving remeshing procedures (e.g., Tvergaard, 1997).

A final important point regarding the quality of the proposed model concerns its validity under various stress triaxiality conditions. Figure 7 shows the variations of the error on $\Delta\varepsilon_n$ as a function of T. The error, on average, decreases when the model is applied to larger stress triaxiality (note that at high stress triaxiality, the fracture strain is small or moderate, and the mesh distortion remains moderate in the cell calculations at the onset of

Table 4. Summary of the equations of the void coalescence model depending on the loading conditions and whether $\gamma_1 = (0.5/\chi_c W_c) > 1$ or $\gamma_1 = (0.5/\chi_c W_c) \leq 1$.

Axisymmetric	if $\gamma_1 \leq 1$	$\Delta\varepsilon_n^{AXI} = \ln\left(1 + \gamma_1\chi_{zc}\left[\dfrac{1 + \chi_{xc}\sqrt{1-\gamma_1^2} - 2\chi_{xc}^2}{2 + (\gamma_1^2 - 1)\chi_{xc}^2 - \sqrt{1-\gamma_1^2}\chi_{xc}}\right]\right)$
	if $\gamma_1 > 1$	$\Delta\varepsilon_n^{AXI} = \ln\left(1 + \dfrac{2\chi_{zc}\chi_{xc}}{3}[2 - \chi_{xc}]\right)$
Plane strain	if $\gamma_1 \leq 1$	$\Delta\varepsilon_n^{PS} = \ln\left(1 + \gamma_1\chi_{zc}\chi_{xc}\exp(\varepsilon_{tr}^c)\left[\dfrac{\chi_{xc}(3-\gamma_1^2)\left(1 - \chi_{xc}\sqrt{1-\gamma_1^2}\right) - \left((2 - \exp(\varepsilon_{tr}^c))/\chi_{xc} - \chi_{xc}^2(1-\gamma_1^2)^{3/2}\right)}{\chi_{xc}\exp(\varepsilon_{tr}^c)\left[(2 - \exp(\varepsilon_{tr}^c))/\chi_{xc} - \chi_{xc}^2(1-\gamma_1^2)^{3/2}\right] - \frac{12}{\pi}\left(1 - \chi_{xc}\sqrt{1-\gamma_1^2}\right)}\right]\right)$
	if $\gamma_1 > 1$	$\Delta\varepsilon_n^{PS} = \ln\left(1 + \dfrac{\pi}{6}\chi_{zc}\chi_{xc}^2\exp(\varepsilon_{tr}^c)\left[2(2 - \exp(\varepsilon_{tr}^c))/\chi_{xc} - 1\right]\right).$

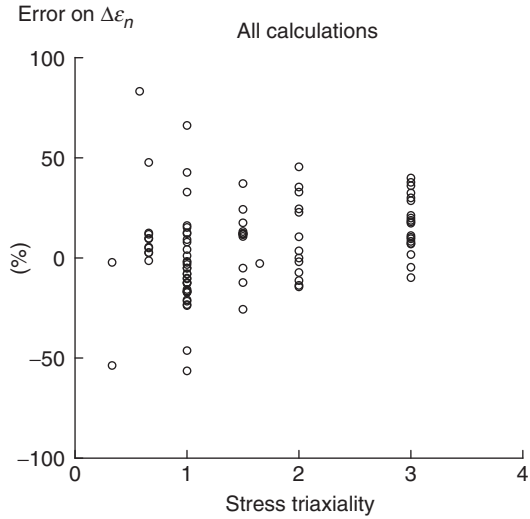

Figure 7. *Evolution of the relative error made on the predicted additional strain increment from onset of coalescence until final fracture as a function of the stress triaxiality.*

coalescence compared to low stress triaxiality problems). A proper description of the coalescence step is especially important at large T because it involves a significant part of the overall dissipation (compare, in Tables 1–3 for large T cases, the ε_n^c and ε_n^f values). This aspect has already been mentioned by Pardoen and Hutchinson (2000, 2003) explaining that inaccurate modeling of the final coalescence step (i.e. of the final unloading stage) in the fracture process zone can lead to large inaccuracies in the predicted cracking resistance. Figure 8 shows the error introduced in the prediction of the fracture strain ε_n^f when relying to the present coalescence model, which remains satisfactory even at large stress triaxiality.

DISCUSSION AND CONCLUSIONS

While recognizing some possible inaccuracies in the extrapolation to final fracture of FE cell calculations used for this assessment, one can however consider that the present coalescence model offers a good trade off between simplicity and accuracy. The model only relies on well defined geometric quantities, which are directly connected to the microstructure of the material and does not introduce any artificial dependence on the loading conditions (stress triaxiality or mode of loading). An extension to general loading conditions can easily be envisaged, but ideally, more advanced or enhanced models should be assessed towards FE cell calculations involving remeshing.

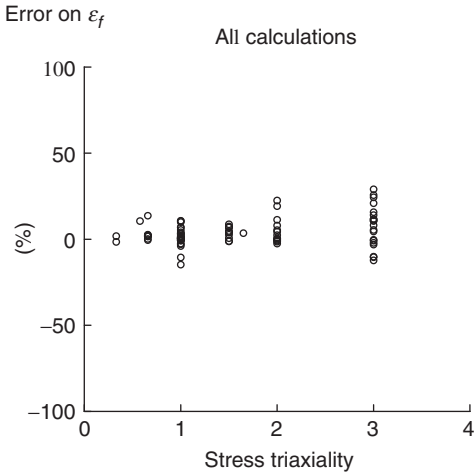

Figure 8. *Relative error made on the predicted final fracture strain as a function of the stress triaxiality.*

By assuming that a void coalescence criterion can accurately predict the stress at the onset of coalescence as well as the state of damage, the present model can be applied as such to simulate the coalescence process through the use, for instance, of a cohesive zone type model for the final unloading step only (section 'Numerical reduction of the load carrying capacity') by predicting the unloading slope $\Delta\sigma_n/\Delta\varepsilon_n$. Now, if the model based on the acceleration of the void growth rate through an effective porosity is used (section 'Phenomenological acceleration of the void growth rate'), the present model can also be used, but would require the identification of the δ factor in Equation (3), such that the target slope $\Delta\sigma_n/\Delta\varepsilon_n$ is properly described (for instance by conducting trials within the FE procedure when making the first increment after the onset of coalescence condition has been reached at a gauss point). In the FE implementation of Scheyvaerts et al. (2009), the slope $\Delta\sigma_n/\Delta\varepsilon_n$ is directly imposed in the constitutive model formulation while enforcing uniaxial constraint in the direction parallel to the predicted orientation of the coalescence band.

Ideally, the use of a void growth model involving void shape effects (such as the extension by Gologanu et al. (1993, 1994, 1997) of the Gurson model) is recommended to correctly capture the onset of void coalescence and to provide a good estimate of W_c and χ_{xc} which enter the coalescence model. Note that, whatever the model, additional error on the fracture strain will thus result from approximations in the void nucleation and void growth laws as well as in the condition for the onset of void coalescence. At the end,

it might be considered that for the sake of reliable structural integrity assessment, the final unloading parameter should be identified directly by inverse modeling through fitting experimental data. Indeed, uncertainty can come during that last stage of the fracture process from different sources, not only from errors inherent to the model, but also from other phenomena not accounted for in the model such as the presence of a second population of voids, microcleavage, crystal plasticity effects. Nevertheless, the present model should be seen as an effort to provide the last brick to a full constitutive model up to final fracture with well defined physical material parameters directly related to the microstructure or plastic behavior. This is essential for guiding materials optimization and/or processing.

NOMENCLATURE

f_0 = Initial void volume fraction
f = Current void volume fraction
f_c = Void volume fraction at the onset of coalescence
f^* = Effective void volume fraction
g_1, g_2 = Fitting functions
h_{zc} = Half height of the localization band at the onset of coalescence
h_{zf} = Half height at final fracture of the band which has, at the onset of coalescence, a half height equal to h_{zc}
L_{x0}, L_{y0}, L_{z0} = Initial void spacing in x, y, and z direction
L_x, L_y, L_z = Current void spacing in x, y, and z direction
L_{xc}, L_{yc}, L_{zc} = Void spacing in x, y, and z direction at the onset of coalescence
R_{x0}, R_{z0} = Initial void radius in x and z direction
R_x, R_z = Current void radius in x and z direction
T = Stress triaxiality
V_c $(=V_f)$ = Volume of the localization band at the onset of coalescence
W_0 = Initial void aspect ratio
W = Current void aspect ratio
α = Fitting factor in coalescence condition varying with strain hardening capacity
χ_0 = Initial relative void spacing
χ = Current relative void spacing
χ_{xc},χ_{zc} = Relative void spacing in the x and z direction at the onset of coalescence
δ = Porosity acceleration factor

$\Delta\varepsilon_n =$ Additional overall strain in the direction perpendicular to the intervoid ligament needed to bring a material element from the onset of coalescence to full final fracture

$\Delta u_z =$ Additional overall displacement in the direction perpendicular to the intervoid ligament needed to bring a material element from the onset of coalescence to full final fracture

$\varepsilon_n^c =$ Overall strain in the direction perpendicular to the intervoid ligament at the onset of coalescence

$\varepsilon_n^f =$ Overall strain in the direction perpendicular to the intervoid ligament at final fracture

$\varepsilon_{tr}^c =$ Deformation in the in-plane direction at the onset of coalescence

$\gamma_1 =$ Geometric factor relating the localization band thickness to the void radius

$\gamma_2 =$ Geometric factor

$\kappa =$ Geometric factor depending on the arrangement of voids

$\lambda_0 =$ Initial anisotropy distribution parameter

$\sigma_z =$ Overall stress in the z direction

$\sigma_n =$ Overall stress in the direction perpendicular to the intervoid ligament

$\sigma_y =$ Current yield stress.

ACKNOWLEDGMENTS

F. Scheyvaerts acknowledges the support of the Walloon Region (DGTRE) and the Fonds Social Européen through a 'FIRST EUROPE Objectif 3' project under the contract EPH3310300R0302/215284. This research has also been carried out under the interuniversity attraction poles programme P6/24, funded by the Belgian State, Belgian Science Policy.

REFERENCES

ABAQUS/Standard version 6.5. User's Manual. Hibbit, Karlsson & Sorensen, Inc. Providence, R.I., U.S. 2004.

Becker, R. (1987). On the Competition Between Particle Fracture and Particle Decohesion in Metal Matrix Composites, *J. Mech. Phys. Solids*, **35**: 577–599.

Becker, R., Needleman, A., Richmond, O. and Tvergaard, V. (1988). Void Growth and Failure in Notched Bars, *J. Mech. Phys. Solids*, **36**: 317–351.

Becker, R., Smelser, E., Richmond, O. and Appleby, E. (1989). The Effect of Void Shape on Void Growth and Ductility in Axisymmetric Tension Tests, *Met. Trans. A*, **20**: 853–861.

Benzerga, A.A. (2000). *Rupture Ductile Des Tôles Anisotropes: Simulation de la Propagation Longitudinale Dans un tube Pressurisé*, PhD Thesis, Ecole Nationale Supérieure des Mines de Paris.

Benzerga, A.A. (2002). Micromechanics of Coalescence in Ductile Fracture, *J. Mech. Phys. Solids*, **50**: 1331–1362.

Benzerga, A.A., Besson, J. and Pineau, A. (1999). Coalescence-controlled Anisotropic Ductile Fracture, *J. Engng Mater. Techn.*, Transactions of the ASME, **121**: 221–229.

Benzerga, A.A., Besson, J. and Pineau, A. (2004a). Anisotropic Ductile Fracture – Part I: Experiments, *Acta. Mater.*, **52**: 4623–4638.

Benzerga, A.A., Besson, J. and Pineau, A. (2004b). Anisotropic Ductile Fracture – Part II: theory, *Acta. Mater.*, **52**: 4639–4650.

Besson, J., Steglich, D. and Brocks, W. (2003). Modeling of Plane Strain Ductile Rupture, *Int. J. Plasticity.*, **19**: 1517–1541.

Brocks, W., Sun, D.Z. and Hönig, A. (1995). Verification of the Transferability of Micromechanical Parameters by Cell Model Calculations with Visco-plastic Materials, *Int. J. Plast*, **11**: 971–989.

Brown, L.M. and Embury, J.D. (1973). In: *Proceedings of the Third International Conference on the Strength of Metals and Alloys*, ICSMA 3, Cambridge, England, pp. 164–169.

Enakoutsa, K., Leblond, J.-B. and Audoly, B. (2005). In: *Proceedings of the 11th International Conference on Fracture*, In: Carpinteri, A. (ed.), March 20-25, Turin, Italy, CD-Rom.

d'Escatha, Y. and Devaux, J.C. (1979). In: Landes, J.D., Begley, J.A. and Clarke, G.A. (eds), *Elastic-Plastic Fracture. American Society for Testing and Materials*, Philadelphia, pp. 229–248 (ASTM STP 668).

Fabrégue, D. and Pardoen, T. (2008). A Constitutive Model for Elastoplastic Solids Containing Primary and Secondary Voids, *J. Mech. Phys. Solids.*, **56**: 719–741.

Gao, X., Faleskog, J. and Shih, C.F. (1998). Cell Model for Nonlinear Fracture Analysis – II. Fracture-process Calibration and Verification, *Int. J. Fract.*, **89**: 374–386.

Gologanu, M., Leblond, J.-B., Perrin, G. et al. (2001). Theoretical Models for Void Coalescence in Porous Ductile Solids. I. Coalescence "In Layers", *Int. J. Solids Struct.*, **38**: 5581–5594.

Gologanu, M., Leblond, J.-B., Perrin, G. and Devaux, J. (1997). Recent Extensions of Gurson's Model for Porous Ductile Metals, In: Suquet, P. (ed.), *Continuum Micromechanics.*, Berlin, Springer-Verlag, Vol. 61.

Gologanu, M., Leblond, J.-B. And Devaux, J. (1994). Approximate Models for Ductile Metals Containing Non-spherical Voids – Case of Axisymmetric Oblate Ellipsoidal Cavities. ASME, *J. Eng. Mater. Technol.*, **116**: 290–297.

Gologanu, M., Leblond, J.-B. and Devaux, J. (1993). Approximate Models for Ductile Metals Containing Non Spherical Voids – Case of Axisymmetric Prolate Ellipsoidal Cavities, *J. Mech. Phys. Solids*, **41**: 1723–1754.

Gullerud, A.S., Gao, X., Dodds Jr, R.H. and Haj-Ali, R. (2000). Simulation of Ductile Crack Growth using Computational Cells: numerical Aspects, *Eng. Fract. Mech.*, **66**: 65–92.

Gurson, A.L. (1977). Continuum Theory of Ductile Rupture by Void Nucleation and Growth: Part I – Yield Criteria and Flow Rules for Porous Ductile Media, *J. Engng Mater. Tech.*, **99**: 2–15.

Huber, G., Brechet, Y. and Pardoen, T. (2005). Void Growth and Void Nucleation Controlled Ductility in Quasi Eutectic Cast Aluminium Alloys, *Acta. Mater*, **53**: 2739–2749.

Hom, C.L. and McMeeking, R.M. (1989). Three-dimensional Void Growth Before a Blunting Crack Tip, *J. Mech. Phys. Solids*, **37**: 395–415.

Koplik, J. and Needleman, A. (1988). Void Growth and Coalescence in Porous Plastic Solids, *Int. J. Solids Struct.*, **24**: 835–853.

Lassance, D., Fabrègue, D., Delannay, F. and Pardoen, T. (2007). Micromechanics of Room and High Temperature Fracture in 6xxx Al Alloys, *Progress. Mater. Sci.*, **52**: 62–129.

Lassance, D., Scheyvaerts, F. and Pardoen, T. (2006). Growth and Coalescence of Penny-shaped Voids in Metallic Alloys, *Engng Fract. Mech*, **73**: 1009–1034.

Leblond, J.-B., Perrin, G. and Suquet, P. (1994). Exact Results and Approximate Models for Porous Viscoplastic Solids, *Int. J. Plast*, **10**: 213–235.

Leblond, J.-B., Perrin, G. and Devaux, J. (1995). An Improved Gurson-type Model for Hardenable Ductile Metals, *Eur. J. Mech. A/Solids*, **14**: 499–527.

Marini, B., Mudry, F. and Pineau, A. (1985). Ductile Rupture of A508 Steel under Nonradial Loading, *Eng. Fract. Mech*, **6**: 989–996.

McClintock, F.A. (1968a). A Criterion for Ductile Fracture by the Growth of Holes, *J. Appl. Mech.*, **35**: 353–371.

McClintock, F.A. (1968b). Local Criteria for Ductile Fracture, *Int. J. Fract.*, **4**: 103–130.

McClintock, F.A. (1971). *Fracture – an Advanced Treatise*, In: Liebowitz, H. (ed.), Academic Press, New York, Vol. 3, pp. 47–225.

Mear, M. and Hutchinson, J.W. (1985). Influence of Yield Surface Curvature on Flow Localization in Dilatant Plasticity, *Mech. Mater*, **4**: 395–407.

Mudry, F. (1982). *Etude de la Rupture Ductile et de la Rupture par Clivage d'aciers Faiblement Allies*, Thése d'Etat, Université de Technologie de Compiégne, France.

Needleman, A. and Tvergaard, V. (1984). An Analysis of Ductile Rupture in Notched Bars, *J. Mech. Phys. Solids*, **32**: 461–490.

Pardoen, T., Doghri, I. and Delannay, F. (1998). Experimental and Numerical Comparison of Void Growth Models and Void Coalescence Criteria for the Prediction of Ductile Fracture in Copper Bars, *Acta. Materialia.*, **46**: 541–552.

Pardoen, T. and Delannay, F. (1998a). Assessment of Void Growth Models from Porosity Measurements in Cold Drawn Copper Bars, *Metall. Mater. Trans. A*, **29A**: 1895–1909.

Pardoen, T. and Delannay, F. (1998b). On the Coalescence of Voids in Prestrained Notched Round Copper Bars, *Fatigue. Fract. Engng Mater. Structures*, **21**: 1459–1472.

Pardoen, T. and Hutchinson, J.W. (2000). An Extended Model for Void Growth and Coalescence, *J. Mech. Phys. Solids*, **48**: 2467–2512.

Pardoen, T. and Hutchinson, J.W. (2003). Micromechanics-based Model for Trends in Toughness of Ductile Metals, *Acta. Mater.*, **51**: 133–148.

Pardoen, T., Dumont, D., Deschamps, A. and Brechet, Y. (2003). Grain Boundary Versus Transgranular Ductile Failure, *J. Mech. Phys. Solids*, **51**: 637–665.

Pardoen, T., Hachez, F., Marchioni, B., Blyth, H. and Atkins, A.G. (2004). Mode I Fracture of Sheet Metal, *J. Mech. Phys. Solids*, **52**: 423–452.

Pardoen, T. (2006). Numerical Simulation of Low Stress Triaxiality Ductile Fracture, *Computers & Structures*, **84**: 1641–1650.

Pardoen, T. and Pineau, A. (2007). *Failure Mechanisms of Metals*, Comprehensive Structural Integrity Encyclopedia, Elsevier, Volume 2, Chapter 6.

Perrin, G. and Leblond, J.-B. (2000). Accelerated Void Growth in Porous Ductile Solids Containing Two Populations of Cavities, *Int. J. Plasticity*, **16**: 91–120.

Ragab, A.R. (2004). Application of an Extended Void Growth Model with Strain Hardening and Void Shape Evolution to Ductile Fracture under Axisymmetric Tension, *Engng Fract. Mech*, **71**: 1515–1534.

Richelsen, A.B. and Tvergaard, V. (1994). Dilatant Plasticity or Upper Bound Estimates for Porous Ductile Solids, *Acta. Metall. et. Mater*, **42**: 2561–2577.

Ruggieri, C., Panontin, T.L. and Dodds Jr, R.H. (1996). Numerical Modeling of Ductile Crack Growth in 3-D using Computational Cell Elements, *Int. J. Fract*, **82**: 67–95.

Scheyvaerts, F., Onck, P.R. and Pardoen, T. (2009). The Growth and Coalescence of Voids under Combined Shear and Tension. *Submitted to J. Mech. Phys. Solids*.

Steglich, D. and Brocks, W. (1997). Micromechanical Modelling of the Behaviour of Ductile Materials Including Particles, *Comput. Mater. Sci.*, **9**: 7–17.

Thomason, P.F. (1968). A Theory of Ductile Fracture by Internal Necking of Cavities, *J. Institute. Metals*, **96**: 360–365.

Thomason, P.F. (1990). *Ductile Fracture of Metals*, Pergamon Press, Oxford.

Thomson, C.I.A., Worswick, M.J., Pilkey, A.K. and Lloyd, D.J. (2003). Void Coalescence Within Periodic Clusters of Particles, *J. Mech. Phys. Solids*, **51**: 127–146.

Tvergaard, V. (1981). Influence of Voids on Shear Band Instabilities Under Plane Strain Conditions, *Int. J. Fract.*, **17**: 389–407.

Tvergaard, V. and Needleman, A. (1984). Analysis of the Cup and Cone Fracture in a Round Tensile Bar, *Acta. Metall*, **32**: 157–169.

Tvergaard, V. (1990). Material Failure by Void Growth to Coalescence, *Adv. Appl. Mech*, **27**: 83–151.

Tvergaard, V. (1997). Studies of Void Growth in a Thin Ductile Layer Between Ceramics, *Comput. Mech.*, **20**: 186–191.

Weck, A., Wilkinson, D.S., Maire, E. and Toda, H. (2008). Visualization by X-ray Tomography of Void Growth and Coalescence Leading to Fracture in Model Materials, *Acta Materialia*, **56**: 2919–2928.

Worswick, M.J., Chen, Z.T., Pilkey, A.K., Lloyd, D. and Court, S. (2001). Damage Characterization and Damage Percolation Modelling in Aluminum Alloy Sheet, *Acta. Mater.*, **49**: 2791–2803.

Xia, L. and Shih, C.F. (1995a). Ductile Crack Growth - I. A Numerical Study using Computational Cells with Microstructurally based Length Scales, *J. Mech. Phys. Solids*, **43**: 233–259.

Xia, L. and Shih, C.F. (1995b). Ductile Crack Growth-II. Void Nucleation and Geometry Effects on Macroscopic Fracture Behavior, *J. Mech. Phys. Solids*, **43**: 1953–1981.

Xia, L., Shih, C.F. and Hutchinson, J.W. (1995). A Computational Approach to Ductile Crack Growth Under Large Scale Yielding Conditions, *J. Mech. Phys. Solids*, **43**: 389–413.

Xia, L. and Shih, C.F. (1996). Ductile Crack Growth-III. Transition to Cleavage Fracture Incorporating Statistics, *J. Mech. Phys. Solids*, **44**: 603–615.

Zhang, Z.L. and Niemi, E. (1995). A New Failure Criterion for the Gurson-Tvergaard Dilational Constitutive Model, *Int. J. Fract.*, **70**: 321–334.